Micro-abrasion-corrosion maps of 316L stainless steel in artificial saliva

A. Hayes, S. Sharifi and M.M. Stack*
Department of Mechanical and Aerospace Engineering, University of Strathclyde, Glasgow, UK.

*Corresponding author. E-mail address: Margaret.stack@strath.ac.uk

Keywords: 316L stainless steel, artificial saliva, oral cavity, abrasion, corrosion, tribo-corrosion mechanisms

Abstract

The role of salivary media is essential during mastication and ingestion processes; yet it can hinder the performance of foreign materials in the oral cavity. The aim of this study was to examine the effects of applied load and applied electrical potential on the tribo-corrosion mechanisms of 316L stainless steel in an environment similar to oral cavity conditions. 316L stainless steel is a material commonly used in dentistry for orthodontic braces, wires and in some cases as dental crowns. This is due to its favourable corrosion resistance. Relatively few studies have examined the materials performance in an oral environment. The results of this work were used to generate polarisation curves and wastage and mechanism maps to describe the material's tribo-corrosion behaviour. A significant difference in corrosion current densities was observed in the presence of abrasive particles suggesting the removal of the protective chromium oxide passive film. It was found that the corrosion resistant nature of 316L stainless steel made its wear mechanism micro-abrasion dominated for all test conditions.

Nomenclature			
A	Surface area of wear scar (m^2)	K_{ac}	Total weight loss (g)
a	Radius of wear scar (m)	K_c	Corrosion weight loss (g)
b	Scar diameter (m)	K_{co}	Pure corrosion weight loss (g)
b_0	Pure abrasion scar diameter (m)	L	Total sliding distance (m)
D	Abrasive particle diameter (m)	M	Atomic mass
E	Applied electrical potential (mV)	R	Cratering ball radius (m)
F	Faraday's constant, 96500 (C mol^{-1})	R_a	Surface roughness (arithmetic average) (µm)
H	Hardness (Pa)	ρ	Sample density (kgm^{-3})
H'	Combined hardness (of surface 1 & 2) (Pa)	S	Coefficient of Severity
I_{corr}	Corrosion current density (mA cm^{-2})	t	Experiment duration (sec)
$I_{corr\,0}$	Pure corrosion current density (mA/cm^2)	V	Volume loss (m^3)
k	Wear coefficient	v	Volume fraction
K_a	Abrasion weight loss (g)	W	Applied load (N)
K_{ao}	Pure abrasion weight loss (g)	Z	Number of valence electrons in corrosion

1. Introduction

The oral cavity represents a significantly challenging environment in materials science. One of the main existing elements in the oral cavity, which can sometimes be overlooked by the material scientists, is saliva and its important roles. During the mastication and ingestion processes, the role of salivary media is multi-faceted i.e. saliva functions as a taste compound diffuser, a lubricant for oral surfaces, a biochemical agent for food structure and an essential ingredient for bolus formation and safe ingestion [1]. The surfaces in the oral cavity can compromise of foreign materials, such as dental replacement and orthodontic materials, which are constantly surrounded by the salivary media. The interactions between saliva and these foreign materials can affect the tribo-corrosion performance.

There are various types of advanced ceramics, metals and polymers that have been employed in modern dentistry, all of which possess many different physical, chemical and aesthetic properties. 316L stainless steel (AISI classification) is one of the longest serving materials in dentistry. The corrosion resistance and mechanical properties of 316L stainless steel make it a desirable option for short to medium term use in the human body. The most common dental implementation of 316L is in orthodontics where it is used to make wires, brackets and bands for braces [2]. The low cost and low toxicity of 316L also make it a favourable choice for longer term implants in developing countries where it is commonly used to make dental crowns.

In recent years, there has been a significant increase in the number of studies examining the tribo-corrosion properties of materials with medical/dental applications. In some recent studies, micro-abrasion and corrosion mechanisms of 316L stainless steel in various solutions, including artificial saliva, have been examined. No studies have however explicitly focused on the synergistic effects of micro-abrasion and corrosion mechanisms which take place on 316L stainless steel in an artificial saliva solution [2]–[6].

The purpose of this study is to identify the occurring tribo-corrosion mechanisms where 316L stainless steel is exposed to an environment which is similar to the oral cavity. This has been achieved through conducting micro-abrasion-corrosion tests in an artificial saliva solution. The research results were then analysed and interpreted through tribo-corrosion maps.

2. Experiment Details

2.1 Test Samples

The dimensions of the 316L stainless steel samples were chosen to be 30 mm in length and breadth, with a thickness of 5 mm to fit the test apparatus platform. The samples were ground

prior to the tests in order to provide a good quality of surface finish. The flatness was confirmed by taking R_a measurements using a Surftest SV-2000 (Mitutoyo, Japan). The density of the samples was confirmed experimentally to be 7.99e6 g/cm^3. The chemical composition (Table 1) of the samples was confirmed using energy dispersive X-ray spectroscopy analysis (EDX).

Element	Weight %
Carbon, C	0.03 (max)
Manganese, Mn	2.00 (max)
Phosphorus, P	0.03 (max)
Sulphur, S	0.03 (max)
Silicone, Si	0.75 (max)
Nitrogen, N	0.1 (max)
Chromium, Cr	17 - 20
Nickel, Ni	12 - 14
Molybdenum, Mo	2 - 4
Iron, Fe	Bal.

Table 1 – Chemical composition of 316L stainless steel

Compound	Concentration (gl^{-1})
NaCl, ***Sodium Chloride***	0.4
KCl, ***Potassium Chloride***	0.4
$CaCl_2 2H_2O$, ***Calcium Chloride Dihydrate***	0.795
$NaH_2PO_4 2H2O$, ***Sodium Dihydrogen Phosphate Dihydrate***	0.78
Na_2S9H_2O, ***Sodium Sulfide Nonahydrate***	0.005
CH_4N_2O, ***Urea***	1
Deionised Water	Bal.

Table 2 – Chemical composition of artificial saliva [7]

2.2 Test Slurry

The original artificial saliva solution was introduced by Takao Fusayama; however, the composition of the solution has evolved over the years. The composition used for this study is reported in Table 2 [7]. It contained electrolytes that can react with metal alloys in a similar manner to natural saliva and had an approximate pH of 5.5 [6]. Saliva is a complex organic solution made up of 99% water; the remaining composition is composed of many inorganic ions (electrolytes), organic compounds (enzymes, antivirals, antibacterials etc.) and proteins which provide a large range of essential functions. Although saliva has a neutral acidity (pH of 7), due to the acidity of the modern western diet, saliva usually becomes acidic during mastication (pH 5 to 6). It is not uncommon for proteins, antibacterial agents and enzymes to be added to artificial organic solutions [8]. Yet these components are unlikely to play a major role in the micro-abrasion-corrosion mechanisms of stainless steel during mastication. They have therefore not been included in the solution used in this study.

The artificial saliva solution was mixed with alumina particles (calcined aluminium oxide powder, Logitech, UK) to form the abrasive slurry. This combination simulates the bolus formation during mastication. Alumina particles were chosen due to the hardness of the

particles. The hardness of the particles can increase the severity of the tests, and high hardness values have been reported for some foods such as nuts [9], [10]. Previous works examined the effects of particle size and concentration [11]–[13]. For these tests, a concentration of 30 gl^{-1} of particles with the average size of 9 µm was used to maintain the consistency with the previous studies [3], [6], [14]. The abrasive particles were kept suspended using a mechanical stirrer during the testing and the solution was replaced after a maximum of one hour testing. Table 3 contains the mechanical properties of the test materials.

Material	Test Function	Density (kgm^{-3})	Hardness (Vickers) [GPa]	Young's Modulus (GPa)	Fracture Toughness (MPa $m^{-1/2}$)
AISI 316L SS	Test Sample	7990	(195) [1.912]	192	100
Alumina	Abrasive Particles	3800	(2035) [1.912]	351	3.5 - 6
UHMWPE	Cratering Ball (counter surface)	931 - 935	(541) [5.306]	0.689	3.5

Table 3 – Test material mechanical properties [10], [15], [16]

2.3 Experiment Apparatus

For this testing a TE-66 Micro-Scale Abrasion Tester (Phoenix Tribology, Reading, UK) was used which operates in accordance with British Standards EN 1071-6: 2007 (Figure 1). This tester generates round wear scars on the samples using a rotating cratering-ball. The test slurry is fed over the contact interface between the sample and the cratering-ball using a peristaltic pump connected to an axel that holds the cratering-ball in place. This axel is driven by a variable speed DC motor. The test slurry is collected in a solution bath below the contact surface. The load between the sample and the counter-body was applied using a stack of dead weights. Here, the load can be finely adjusted using an adjustable counter-weight.

UHMWPE (ultra-high-molecular-weight-polyethylene) balls (K-mac Plastics, Michigan, USA) with the diameter of 25.4 mm (1 inch) were used for these tests. UHMWPE possesses a very low friction coefficient and high wear resistance which significantly reduces the interference of the ball in the wear process [15]. UHMWPE is a non-conductive material and therefore has no effects on the corrosion currents. The sliding velocity of the tests was kept constant. Three balls were used during the tests. After each test the balls were measured for deformation, visually inspected for contamination, cleaned with deionised water. In addition, the balls were incrementally turned in their fixings after each test to prevent any deformation of the spherical

shape of the balls. The careful and measured reuse of UHMWPE balls is an economic compromise that has been adopted in other micro-abrasion studies [6], [17].

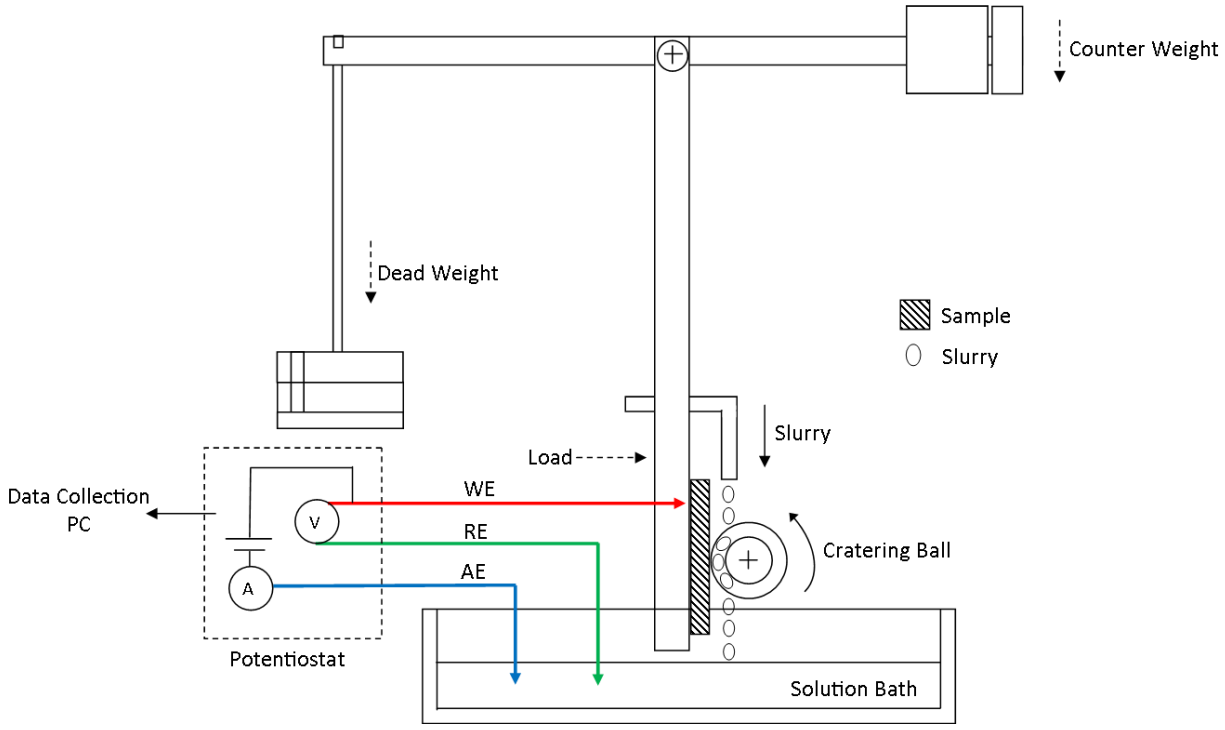

Figure 1 – TE-66 Micro-Scale Abrasion Tester

A potentiostat (ACM Instruments, UK) was used to apply electrical potentials to the samples and measure the corrosion currents. The working electrode (WE) was fixed to the back of the test samples and the auxiliary (AE) and reference electrodes (RE) were placed in the solution bath. The test samples were insulated using non-conductive tape with a 1 cm^2 square section left uncovered. It should be noted that these tests were not conducted in a de-aerated condition.

2.4 Test Methodology

These tests were conducted to examine the effects of applied load and applied electrical potential on tribo-corrosion mechanisms of 316L stainless steel. As shown in Table 4, the test matrix consisted of 5 different applied loads and 5 electrical potentials. Several recent studies have been conducted to examine the particle size and distribution properties of food bolus of varying hardness [11], [18]. Chen et al and Jalabert-Malbos et al have reported that the forces

required to break the food into bolus, ranges from 0.06 N for egg whites to 24 N for roasted peanuts with the majority of common foods requiring less than 5N. Hence, a load range of 0.5 to 4 N has been chosen for the tests.

Also, the highest and the lowest reported intraoral potentials in the literature are -431 and +300 mV [19]. As a result, the selected range of the electrical potentials for these set of experiments were from -600 mV to 200 mV to reflect the earlier findings and the condition changes from cathodic to anodic [6].

The performance of 316L in pure abrasion conditions for each applied load was also investigated. For this purpose, an applied potential of -960mV was used to provide a cathodic protection condition for the samples [20]. To study the effects of the presence of the particles in the solution, cyclic sweep tests were also conducted for each load, with and without particles, which produced the polarisation curves. The cyclic sweep polarisation tests lasted 30 minutes and applied an electrical potential from -1000mV to 500mV with the sweep rate of $50mVs^{-1}$.

The cratering-ball was rotating at the speed of 150 rpm for the duration of 30 minutes. The combination of the rotational speed and test length resulted in a total sliding distance of 359 m per test. Previous studies have shown that the average sliding distance per tooth each day is approximately 1 meter. Thus, each test approximates 1 year of material use as a crown [14].

Test conditions	
Applied loads (N)	0.5, 1, 2, 3, 4
Applied electrical potentials (pure abrasion tests) (mV)	(-960), -600, -400, -200, 0, 200
Sliding speed (rpm)	150
Sliding distance (m)	≈ 359
Test duration (mins)	30
Cyclic Sweeps	0.5, 1, 2, 3, 4 N (with and without particles)

Table 4 – Test conditions

The test outcomes were cross-referenced with the previous studies. Therefore, only the tests with abnormal outcomes were repeated in order to confirm the reproducibility. The abnormal results due to the probable occurrence of errors are not reported or used to create averages and scatterings. To avoid errors in the calculations, all were done in excel without rounding.

3. Results

3.1 Polarisation Curves

Figures 2(a) and 2(b) are the polarisation curves generated from the cyclic sweep tests for all applied loads, both without and with particles. Figure 2(a) displays more uniformity in corrosion current densities for all loads in the absence of abrasive particles. This is in comparison with Figure 2(b) where the abrasive particles are present. It can be seen that the corrosion current densities for the tests with particles are higher than the tests without particles. With the exception of 0.5N during cathodic conditions, all the corrosion currents densities are almost ten times greater with particles than without particles.

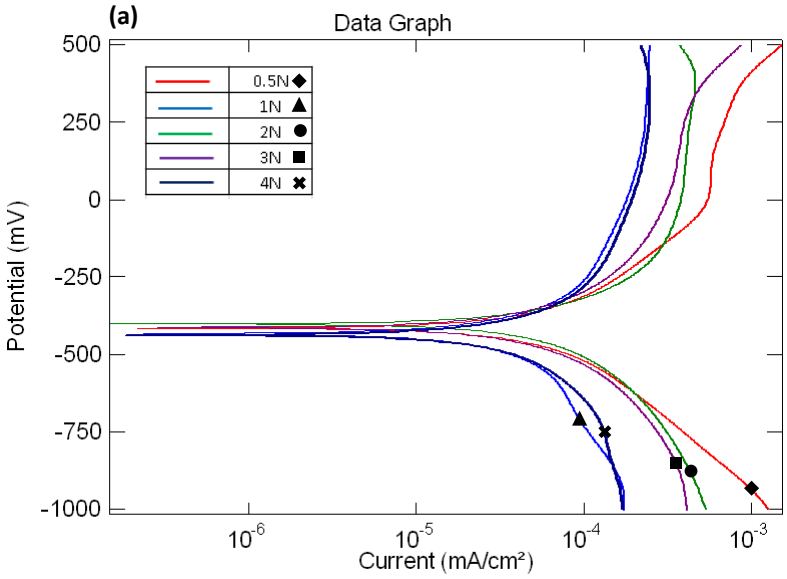

Figure 2(a) – Polarisation tests without particles

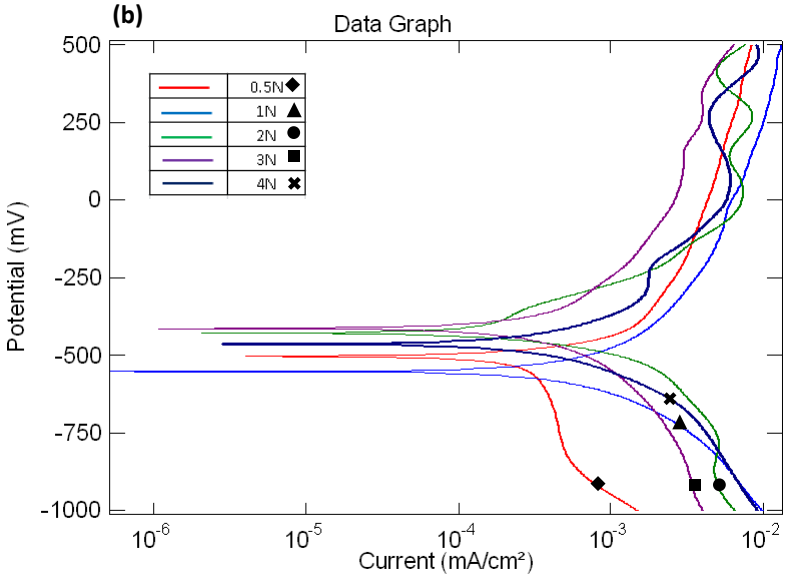

Figure 2(b) – Polarisation tests with particles

3.2 Alumina particles

In order to have a better understanding of the function of the alumina particles in the tests, a small amount of the fresh particles was compared with the used particles collected from the solution bath. The images were taken using a S3700 (Hitachi, Japan) Tungsten Filament Scanning Electron Microscope (SEM). As shown in Figure 3, the size of the particles did not seem to be altered after the test. This confirmed the validity of the particles material selection to avoid degradation. If the hardness of the abrasive particles and the target surface are relatively close, the wear rate can vary due to the occurrence of a phenomenon known as 'soft abrasion'. This takes place when the hardness of the abrasive particles alters during the interaction [21]. It should be noted that the size values in the two images are there to facilitate the comparison.

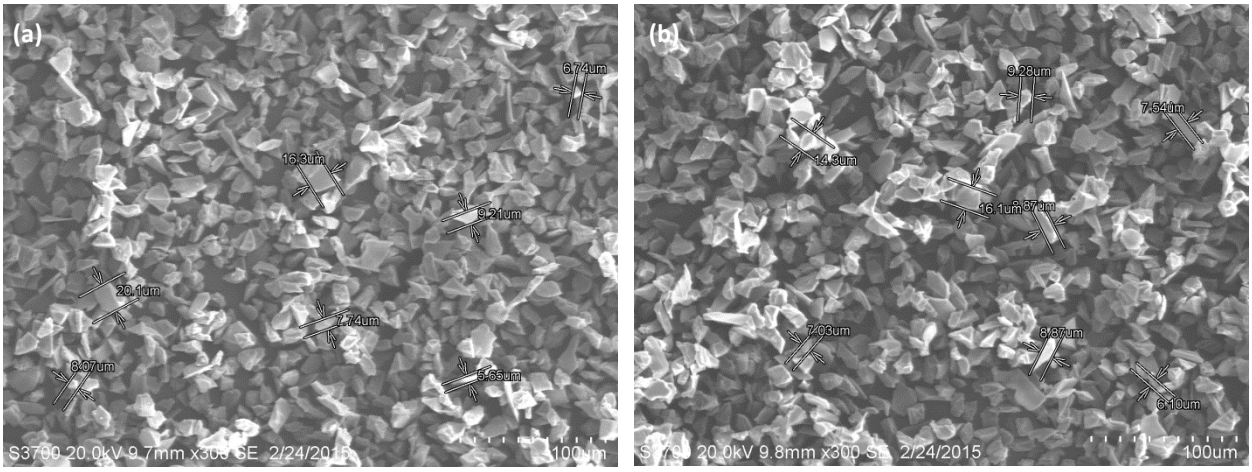

Figure 3 – Particle distribution (a) before and (b) after testing

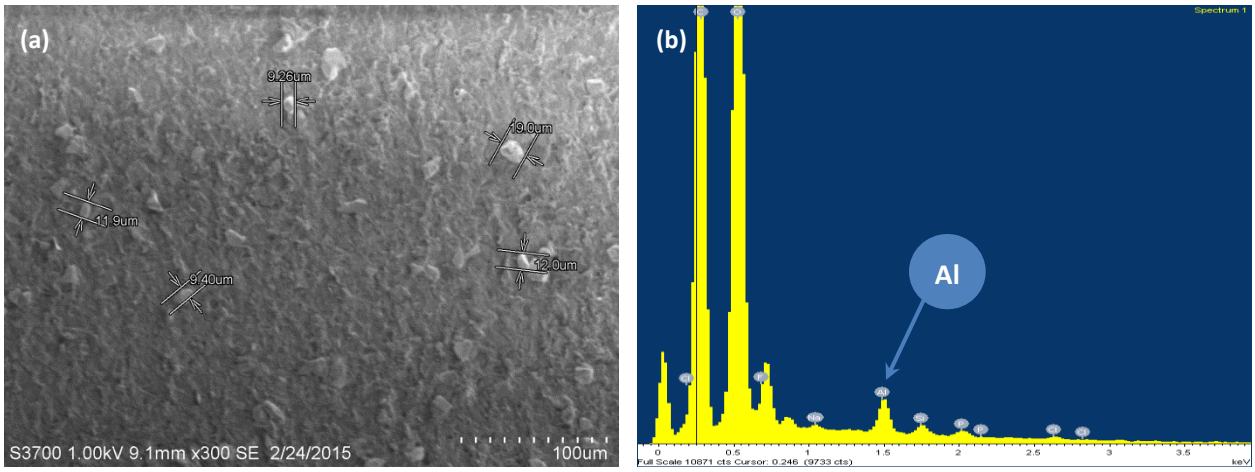

Figure 4 – Particle embedment on the cratering ball surface after testing (a) SEM image (b) EDX analysis

The cratering ball was also inspected, after a test and before cleaning, for the occurrence of particle embedment on the ball surface. As depicted in Figure 4, the embedment was observed on the surface and this was confirmed using EDX analysis. The embedment of particles on the cratering surface increases the tendency of transition of the abrasion mechanism from 3-body rolling towards 2-body-grooving [22].

3.3 Wear scars

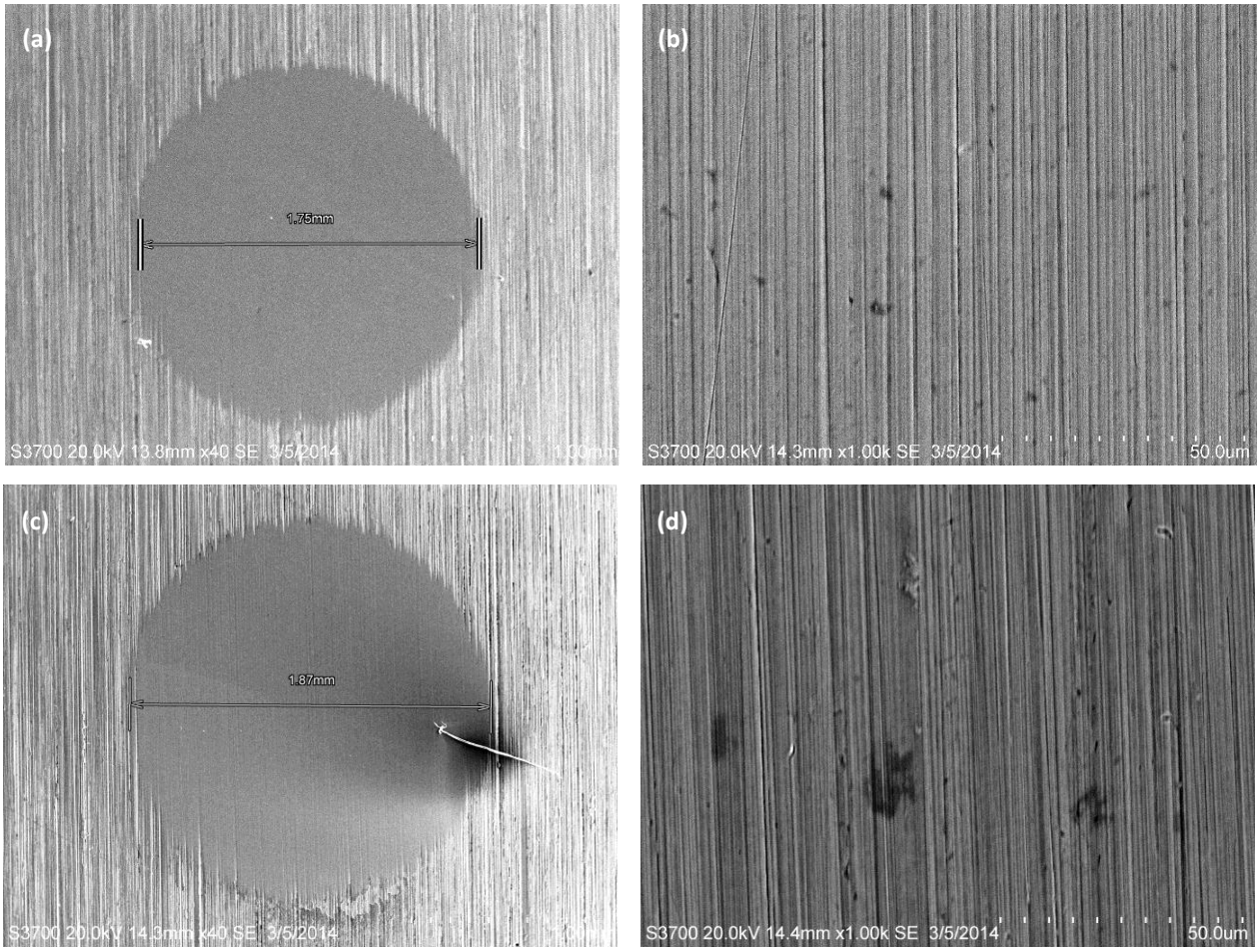

Figure 5 - SEM micrographs of the wear scar from the cyclic sweep tests with particles at (a) 0.5N wear scar diameter x40, (b) 0.5N magnified scar x1000, (c) 2N wear scar diameter x40 and (d) 2N magnified scar x1000

Scanning Electron Microscopy (SEM) was used to measure the wear scar diameters and take micrographs to identify the wear mechanisms which created the scars. As expected and demonstrated in Figure 5, the dominant wear mechanism was 2-body grooving in all cases. The only difference between the scars was the severity which resulted in the variation of the material loss. Figure 5 represents an example of this similarity. It was also noted that none of the SEM micrographs appeared to show any visual signs of surface corrosion. Although this was

consistent with the previous studies findings [3], [6], after completing the SEM, a number of samples were cut through the scars and mounted to investigate the cross-section of the scars. This provided an opportunity for the inspection of the cross-sectional shape of the scars, existence of corroded layers on the. Figure 6 exhibits the images that were taken from the scars cross-sections using an optical microscope (Olympus GX51, Japan). Figure 6(a) confirms the hemispherical shape of the scars. By increasing the magnification and focusing in the middle area of the scars, it was still not possible to identify any clear corrosion layers. This can be due to the lower mass of corrosion wear recorded comparing to the mechanical wear. This is discussed in detail in the next section. From the microscopy results, it was also noted that the substrate material did not exhibit any form of uninform corrosion or pitting. Figure 6(c) shows the difference between the sample surface and the scar surface and Figure 6(d) is a cross-section of the grooves on a scar surface.

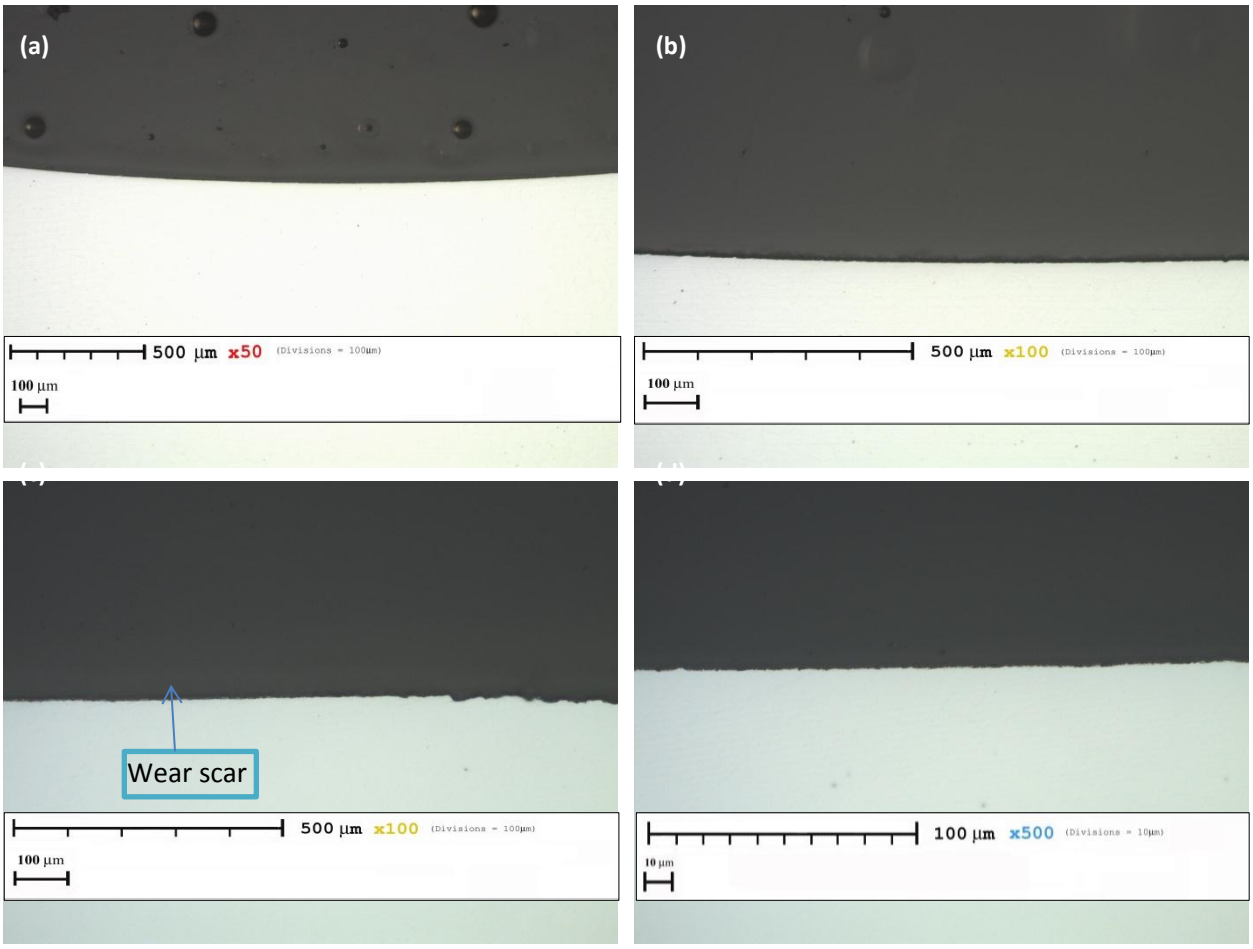

Figure 6 – Optical microscopy images from the scars cross-sections (a) 0.5N -600mV - full scar, (b) 2N cyclic sweep test with particles- full scar, (c) 2N -400mV - scar edge and (d) 0.5N -600mV middle area

3.4 Weight loss

The wear scars created during testing were analysed using the method developed by Yue and Shi [20]. For each test, the total weight loss (K_{ac}) was divided into weight loss due to micro-abrasion (K_a) and to corrosion (K_c).

$K_{ac} = K_a + K_c$ (1)

The total weight loss (K_{ac}) was calculated by multiplying the density of the sample material and the volume loss (V) which can be calculated using equation (2) as the hemispherical shape of the scars was confirmed in the previous section [23]:

$V = \frac{\pi b^4}{64R}$ (when $b<<R$) (2)

V = Volume loss
b = Diameter of wear scar (m)
R = Cratering ball radius (m)

The corrosion weight loss (K_c) was calculated using a variation of Faraday's Law:

$K_c = \frac{MI_{corr}t}{ZF}$ (3)

K_c = corrosion weight loss (g)
M = Atomic mass
I_{corr} = Corrosion current density [mA cm-2]
t = Experiment duration (sec)
Z = Number of Valence Electrons
F = Faraday's Constant, 96500 (C mol^{-1})

Micro-abrasion weight loss (K_a) can also be divided up into pure micro-abrasion weight loss (K_{ao}) and the synergistic effect of corrosion on the micro-abrasion (ΔK_a):

$K_a = K_{ao} + \Delta K_a$ (4)

The pure micro-abrasion weight loss (K_{ao}) was calculated using equation (2), the material density and the wear scars from the pure micro-abrasion tests (cathodic conditions at -960 mV) for each applied load.

Similarly, corrosion weight loss (K_c) can be divided up into pure corrosion weigh loss (K_{co}) and the additive effect of micro-abrasion on the corrosive weight loss (ΔK_c):

$K_c = K_{co} + \Delta K_c$ (5)

Approximate values of pure-corrosion weight loss (K_{co}) were calculated using equation (3) and the 'I_{corr}' values from the polarisation curves without particles (I_{corr0}) for every applied load and each electrical potential.

(a)

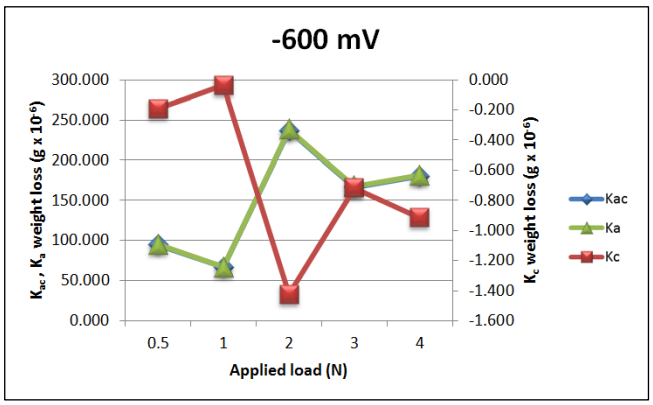

(b)

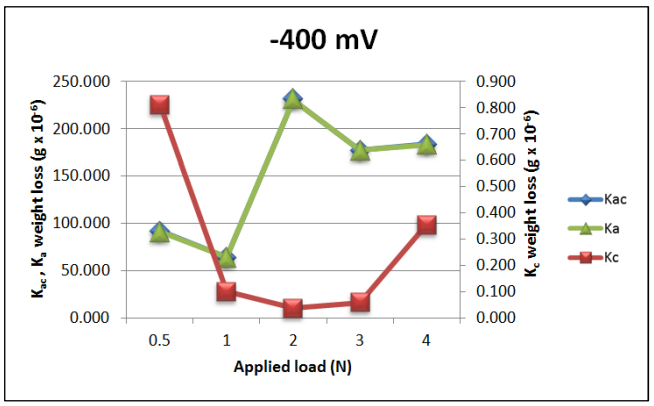

(c)

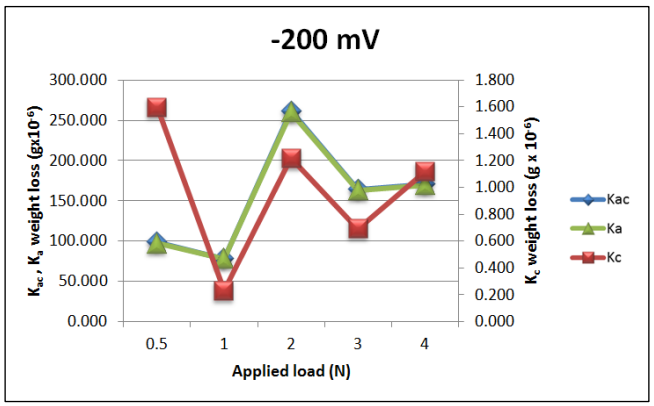

(d)

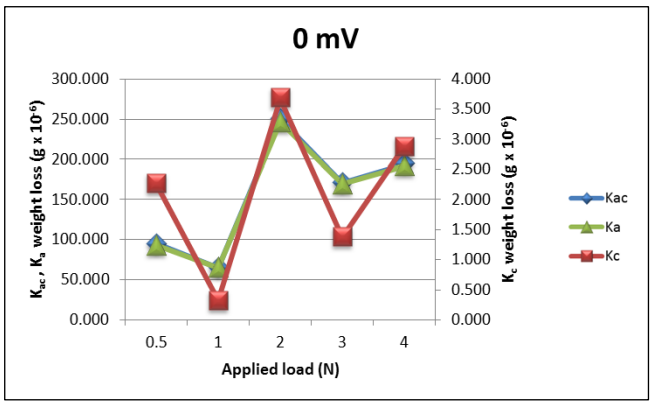

(e)

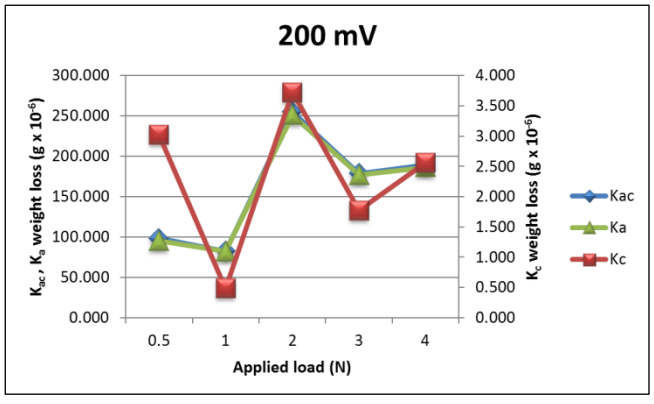

Figure 7 – Weight loss graphs of 316L stainless steel for the load range of 0.5 - 4 N at (a) -600 mV, (b) -400 mV, (c) -200 mV, (d) 0 mV, and (e) +200 mV.

Figure 7 presents the calculated total weight loss (K_{ac}), the micro-abrasion weight loss (K_a) (LHS axes), and the corrosion weight loss (K_c) (RHS axis) results. It should be noted that the scales of the LHS axes are much higher than the RHS ones. The results show that for every test condition the total and micro-abrasion weight loss values are very close in magnitude, whilst the corrosion weight loss is much less. There is also very little variation in total/micro-abrasion weight loss for each load over a range of applied potentials. For each applied load the corrosion weight loss increases with increasing applied potential. There is only a very small increase in abrasion weight loss when corrosion is included ($K_{ao} >> \Delta K_a$). Yet the corrosion is roughly ten times greater when abrasion is included ($K_c \approx 10K_{co}$).

4. Discussion

The ability to predict wear of materials is a universal challenge crucial to successful application of new materials into different technologies. There are numerous methods to describe wear data such as tabulated wear rates or elucidation of the dominant wear mechanisms using micro-graphs [24]. Of all these methods, a more comprehensive method is to link the wear rates and wear mechanisms in a much wider range of sliding conditions known as 'wear maps'. There are a limited number of standardised wear testing methods and often the variables of a study are incomparable with one another. Hence, wear (mechanism) maps can be an extra-ordinary informative tool to link mechanisms to operating parameters [25].

4.1 Tribo-corrosion maps

Wastage and mechanism maps were generated for 316L stainless steel using the test results (with particles) and mapping techniques have been developed in previous studies [26], [27]. The maps were drawn by plotting the results of the 25 tests on a chart and interpolating between the points to determine the boundary lines. It had to be assumed that the wear results varied linearly between each condition.

For the wastage map (Figure 8) the categories of wear were taken from previous studies [3], [6], [14], [20] and adapted as follows:

	Very Low:			K_{ac}	$\leq$	$0.15 * K_{ac\ max}$
	Low:	$0.15 * K_{ac\ max}$	$<$	K_{ac}	$\leq$	$0.35 * K_{ac\ max}$
	Medium:	$0.35 * K_{ac\ max}$	$<$	K_{ac}	$\leq$	$0.80 * K_{ac\ max}$
	High:	$0.80 * K_{ac\ max}$	$<$	K_{ac}		

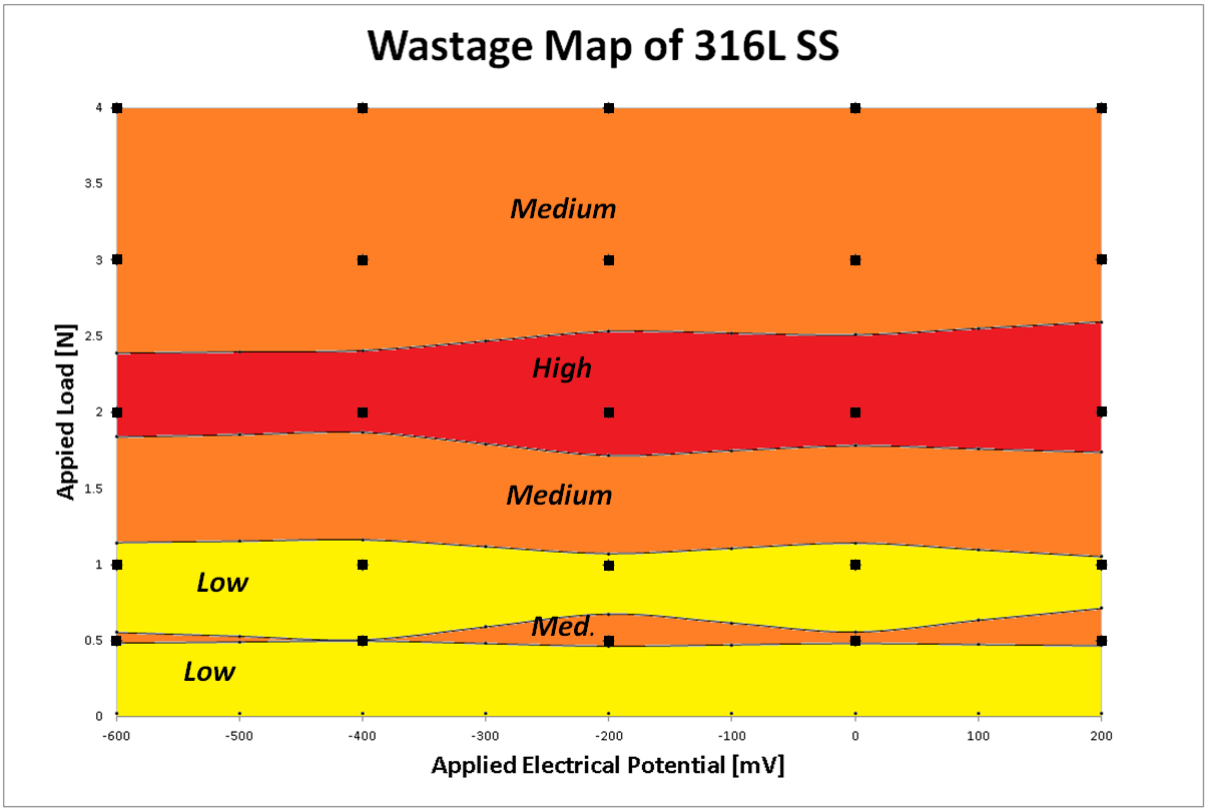

Figure 8 – Wastage map of 316L stainless steel in artificial saliva

The wastage map clearly shows that applied electrical potential had no significant effect on the total wear compared to the applied load. This is due to the fact that the amount of material loss caused by corrosion was much lower than micro-abrasion. As a result, any variation in material loss due to corrosion has no significant effect on total wear. The map shows that the highest wastage occurred at 2N and the lowest wastage occurred at loads lower than 1N.

It was noted that the highest load did not cause the highest material loss. This may be due to entrainment issues associated with abrasive particles at higher loads. Higher loads produce higher pressure in the contact area, which may reduce the frequency of particle entrainment. This may result in unexpected wear rates. Thus, regardless of the type of the surface material and despite the presence of load and abrasive particles, the wear rate may decrease due to entrainment of particles for a period of time. Also, Lansdown and Price [28] and Stack and Mathew [22] have proposed that at higher loads transitions between the wear mechanisms are not unexpected. This suggests that the relation between the material loss and applied load is more complicated than a linear relationship between the applied load and wear rate. Another possible reason for this pattern of behaviour is the duration of the tests. Ridges are generally formed at the early stages of development of the scar and typically do not alter the background profile of the wear crater [29]. Despite of the presence of load and abrasive particles, the wear rate may decrease due to entrainment of particles in the formed ridges. However when the

ridge is eventually removed, a sudden increase is observed in the wear rate. Previous work by the current authors [6] for a similar load range showed the highest wear rate was found to be at 4N load, but this was after 3 hours of testing.

For the mechanism map (Figure 9) the categories of the mechanisms were adopted from the previous work of the group [20]. An additional 'pure micro-abrasion' category was added since the map was micro-abrasion dominated. The categories were as follows:

	Pure micro-abrasion:			K_c/K_a	$\leq$	*0*
	Micro-abrasion:	*0*	$<$	K_c/K_a	$<$	*0.1*
	Micro-abrasion–corrosion:	*0.1*	$\leq$	K_c/K_a	$<$	*1*
	Corrosion–micro-abrasion:	*1*	$\leq$	K_c/K_a	$<$	*10*
	Corrosion:	*10*	$\leq$	K_c/K_a		

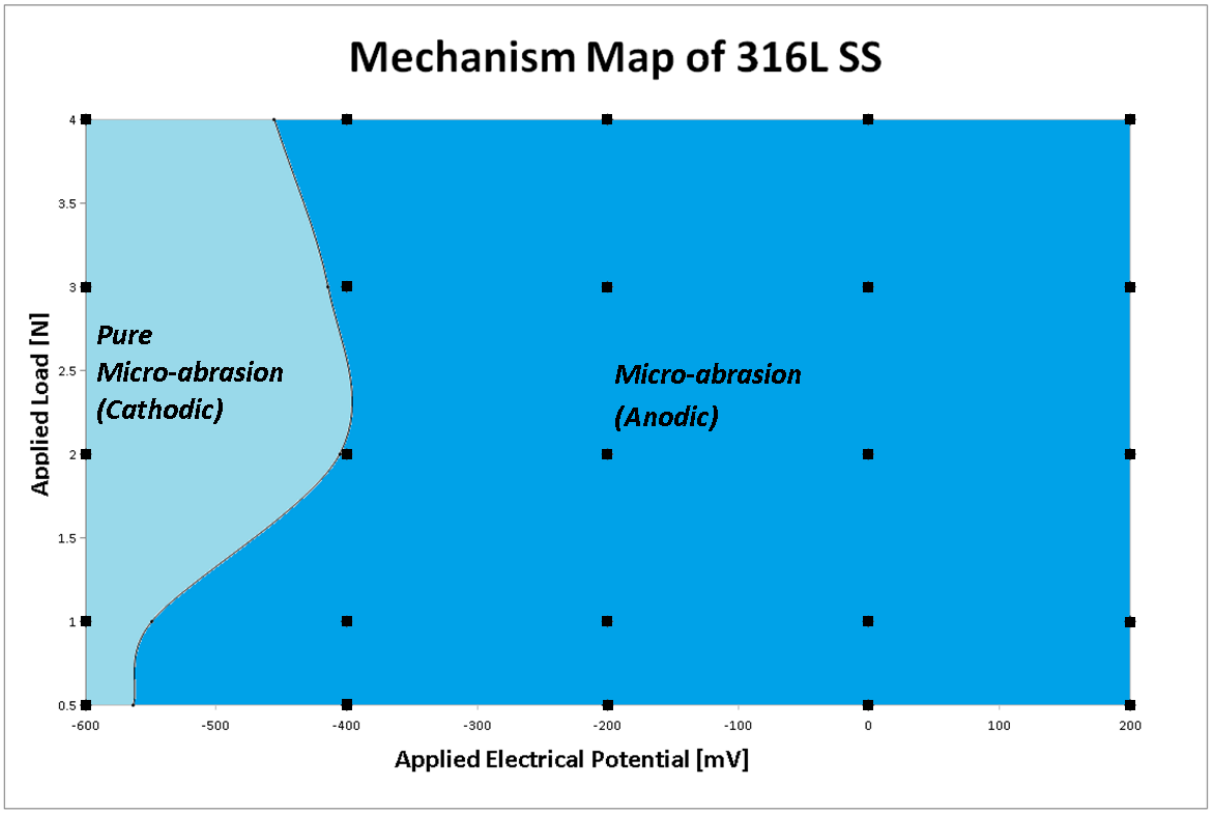

Figure 9 – Mechanism map of 316L stainless steel in artificial saliva

The mechanism map of 316L SS stainless steel shows that the wear mechanism is heavily micro-abrasion dominated. For example, from the results showed that at the highest ratio of corrosion to micro abrasion (0.5N at 200mV), micro-abrasion is still thirty times greater than the corrosion. The mechanism map also highlights that under pure micro-abrasion (cathodic), the highest electrical potential was observed for 2N load and at the lowest for 0.5 and 1N. The

Pourbaix Diagrams for iron and chromium [30] indicated that the corrosion of iron begins at a higher electrical potential than chromium. This suggests that more of the chromium oxide passive film has been removed for loads of 2N compared to 0.5 and 1N. This is consistent with the results displayed in the wastage map that display the highest wastage at 2N and the lowest wastage at load bellow 1N.

4.2 Corrosion and Passive Film Removal

For all applied loads, the corrosion current densities were greater for the cyclic sweeps (polarisation curves) with the presence of abrasive particles than that in their absence (Figure 2). This is an indication that the chromium oxide passive film, which protects the iron from oxidising, had been removed by the abrasion of the alumina particles. This could mean that the corrosion in tests without particles is largely from the chromium reacting with the chloride in the saliva solution, whilst the corrosion in tests with particles is mostly from iron oxidation on the samples' un-protected surface [31].

This can be confirmed by the electrical potential at which passivation occurs and by the presence of repassivation phenomenon observed in the polarisation curves for 2, 3 and 4N with particles (Figure 2(b)). According to the Pourbaix diagram for chromium [30], pure chromium will not passivate in a chloride solution with a pH of 5.5, but in other solutions chromium will passivate at potentials above -500 mV. Since the artificial saliva solution contains a low chloride concentration and non-chloride electrolytes, it can be assumed that the passivation at approximately -500mV in all polarisation curves (Figures 2 (a) and (b)) is a result of the corrosion of the chromium oxide passive film. For iron, the Pourbaix diagram for iron indicates passivation in a solution of pH of 5.5 at applied electrical potentials greater than 300mV. This is a likely explanation for the repassivation phenomena observed in the polarisation curves for 2, 3 and 4N with particles.

The weight loss results (Figure 3) indicate a relationship between the rate of micro-abrasion and corrosion. For applied electrical potentials greater than -200mV (anodic) the rate of corrosion increases when the rate of micro-abrasion increases;conversely the rate of corrosion decreases when the rate of micro-abrasion decreases (Figure 10). This would appear to suggest, that for anodic conditions, when the rate of micro-abrasion increases, the rate at which the chromium oxide passive film is removed also increases resulting in more iron oxidation. If this is correct then there should also be a relationship between the rate of micro-abrasion and presence of repassivation phenomena. Repassivation phenomena can be observed in the polarisation curves of 2, 3 and 4N which are the three loads with the highest micro-abrasion. The loads resulting in the lowest micro-abrasion, 0.5 and 1N, display no repassivation. 2N is the

load with the highest micro-abrasion and it has a greater frequency of repassivation. Of the loads displaying repassivation, 3N has the lowest micro-abrasion and this also has the lowest frequency of repassivation. This suggests that higher rates of micro-abrasion also remove the repassivation film at a higher rate.

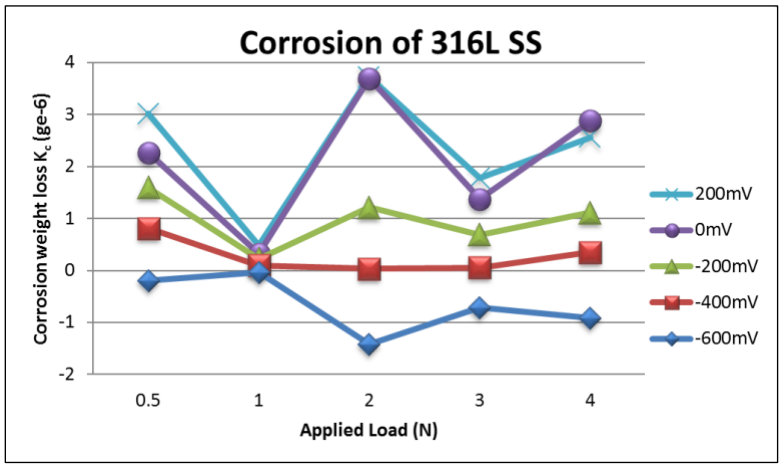

Figure 10 – Graph of corrosion of 316L stainless steel

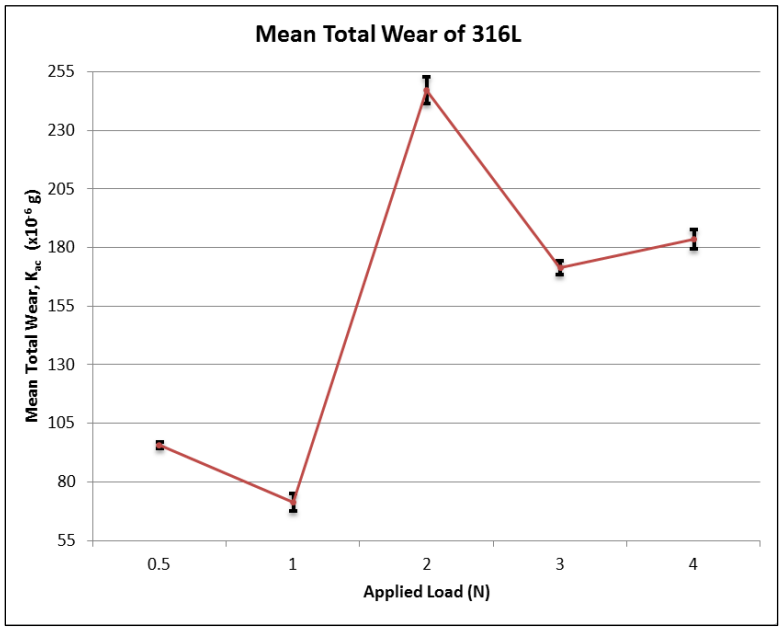

Figure 11 – Mean total wear for all loads with standard error for all applied electrical potentials

4.3 Total Wear

The non-linear relationship between applied load and micro-abrasion observed in this study's results is consistent with a previous study of 316L stainless steel in artificial saliva [6]. Other recent studies of different materials and solutions suggest that applied electrical potential has no observable effect on the rate of micro-abrasion [20]. This conclusion appears to be consistent with the results of this study since the total wear of each applied load is constant for all applied electrical potentials. This can be further confirmed by the graph above (Figure 11)

which displays the mean total micro-abrasion mass change for each applied load with a standard error showing the wear variation over all applied electrical potentials. The 'error' shows a very low variation between the 5 applied electrical potentials. A standard error for every electrical potential cannot be generated because only abnormal (unreportable) test results were repeated.

4.4 Wear Severity Coefficients

In recent literature two different methods have been used to express the severity of total wear. The first is based on the work of J. F. Archard who established an equation to predict the volume loss of a material [32]:

$$V = \frac{KWL}{H} \quad (6)$$

Where '*V*' is the predicted volume loss, '*K*' is a constant dimensionless coefficient of wear, '*W*' is the applied load, '*L*' is the total sliding distance and '*H*' is the hardness of the softer of the two surfaces (in Vickers). If the measured volume loss is used for '*V*', then '*K*' can be calculated for each test condition. Archard's prediction assumes that total wear will increase linearly as load and sliding distance increases. This is has been proven true for adhesive sliding wear and to some extent for hard particle abrasive wear [33], [34]. For non-linear wear '*K*' can then be classed as a measure of severity (Figure 12).

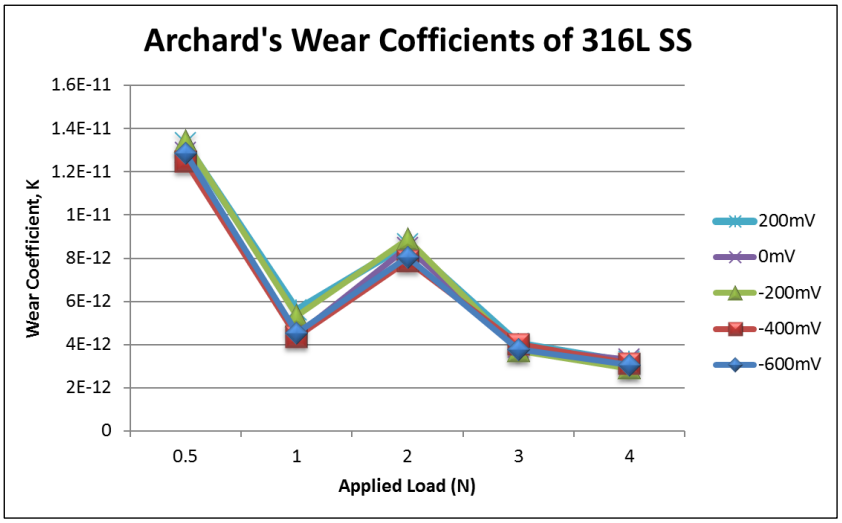

Figure 12 – Archard's coefficient of wear for 316L stainless steel

The results for Archard's wear coefficients show that the coefficients are constant for all applied electrical potentials for each applied load. The results also show a decreasing severity with increasing applied load with the highest severity occurring at 0.5N and the lowest at 4N.

This is likely due to the fact that Archard's prediction assumes that the greatest wear will be observed at higher loads.

The second method for expressing wear severity was established by Adachi and Hutchings [26] and is expressed as:

$$S = \frac{W}{AvH'} \qquad (7)$$

$$\frac{1}{H'} = \frac{1}{H_s} + \frac{1}{H_b} \qquad (8)$$

$$A = \pi(a^2 + 2RD) \qquad (9)$$

Where '*S*' is a dimensionless coefficient of wear severity, '*W*' is applied load, '*A*' is the wear scar surface area, '*v*' is the volume fraction of abrasive particles in the solution, '*H*" is the combined hardness of the sample (H_s) and the cratering ball (H_b) in *Pa*, '*a*' is the radius of the Hertzian contact area, '*R*' is the cratering ball radius and 'D' is the particle diameter. The volume fraction of abrasive particles in the solution '*v*' is 0.03. Using the Hertzian formulae for a ball/flat surface, the contact pressure between the cratering ball and the sample surface varies from 0.35 *MPa* to 2.1 *MPa*. The contact pressure between the abrasive particles and the sample surface will be much higher. For this study the scar surface area was calculated using the scar diameter. This method of expressing the wear severity produces an increasing linear relationship between severity '*S*' and applied load (Figure 13):

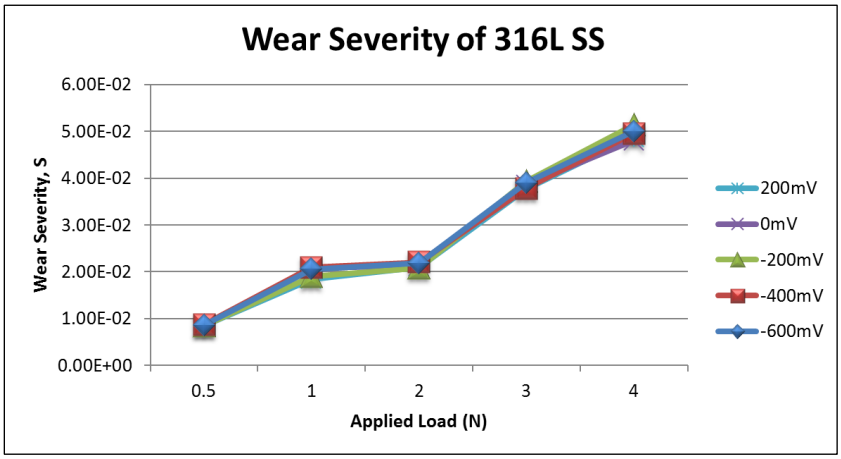

Figure 13 – Wear severity 'S' for 316L SS in artificial saliva

There does not seem to be any clear correlation between wear severity 'S' (Figure 11) and corrosion rate, but it does produce an increasing linear relationship with applied load. There does also appear to be a corresponding relationship between total (micro-abrasive) wear (Figure 11) and corrosion (Figure 10) during anodic conditions. An increase in total wear between load conditions is accompanied by an increase in corrosion rate and conversely a

decrease in total wear is accompanied by a decrease in corrosion rate. Also, by comparing the two methods of evaluating the wear rate (Figures 12 and 13), an existing correlation can be suggested between the Archard wear coefficient and inverse of wear severity:

$$K \propto \frac{1}{S} \qquad (10).$$

4.5 Wear Regimes

As mentioned earlier, the non-linear relationship between applied load and micro-abrasion is largely due to the transitions between different wear regimes. The two simplified classifications of hard particle abrasive wear regimes are two and three-body abrasive wear [21]. More recent studies in abrasion wear regime transitions have established that there are more regimes including mixtures of these wear regimes but the fundamental concepts and classifications of these two modes still hold [17], [22]. It was originally thought that three-body rolling wear occurs at lower loads and this transitions to two-body grooving at higher loads [21]. More recent studies have established that as applied load is increased the wear regime transitions from a mixture of three and two body wear to two body wear and then back to a mixture of three and two body wear [22], [35].

In addition to establishing the calculation for wear severity '*S*', Adachi and Hutchings [26] were also able to quantify the wear severity at which regime transitions occur for a given surface to cratering ball hardness ratio. Based on multiple micro-abrasion test studies of different materials using various abrasive particles and solutions, they proposed that three-body abrasive wear will transition to two-body abrasive wear when:

$$S = \frac{W}{AvH'} > \alpha \left(\frac{H_s}{H_b}\right)^{\beta} \quad (10)$$

Dimensionless constants:
α = 0.0076
β = -0.49

where the notation is the same as for the severity of wear 'S' (Equations 7-9). The surface to cratering ball hardness ratio for 316L SS and UHMWPE is 0.36 (see Table 3). This means, that according to Adachi and Hutchings' prediction, the wear regime is expected to transition from three to two-body wear at a wear severity value of 0.01254. The mean wear severity values for each applied load and the transition conditions are plotted in the Figure 14. According to this prediction three-body wear should be present at 0.5N, two-body wear at loads of 1N and higher and the possibility of a mixed wear regime at 0.5, 1 and 2N. Some of these wear regimes can be confirmed by the SEM micrographs of the wear scars (Figure 15).

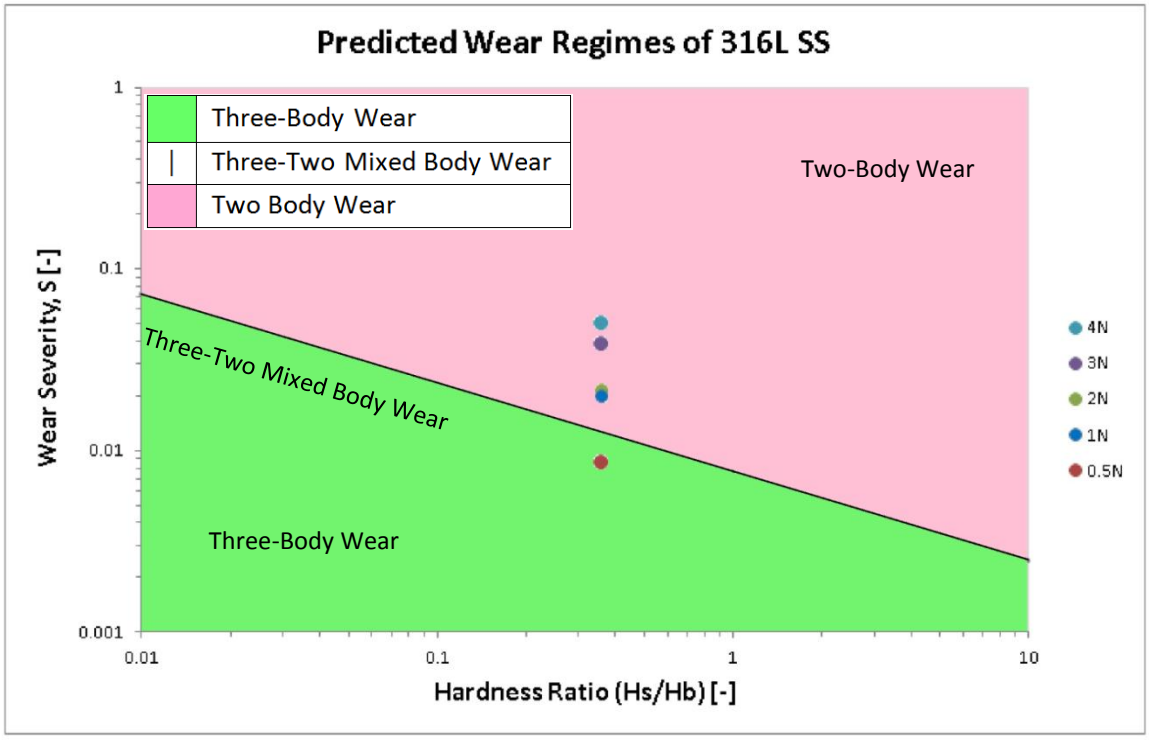

Figure 14 - Predicted wear regimes for 316L SS at different loads

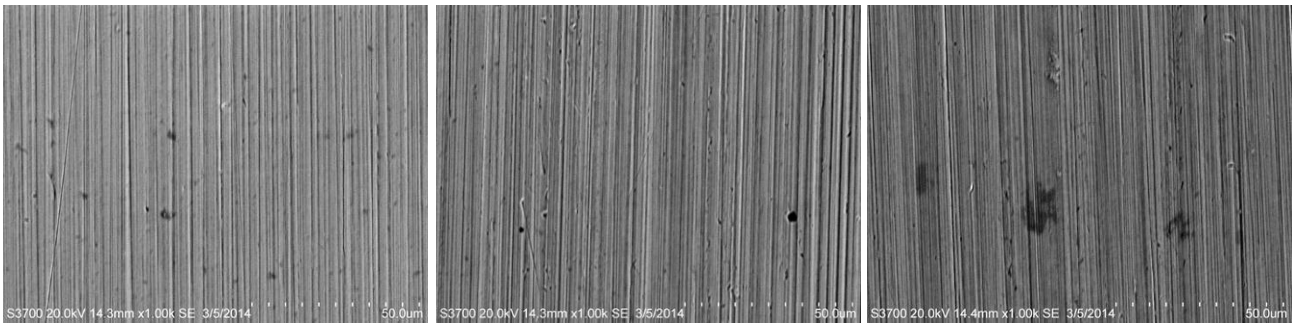

(a) (b) (c)

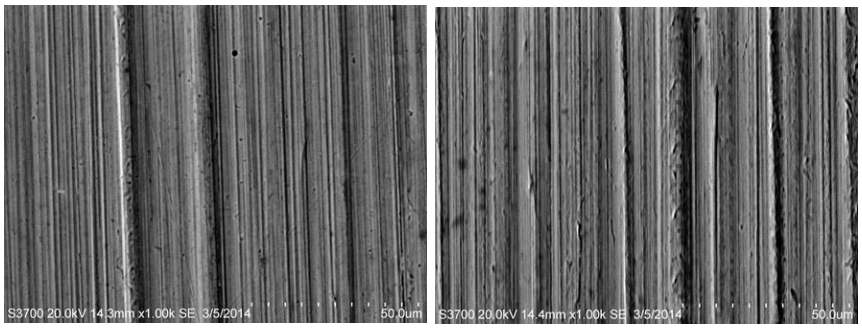

(d) (e)

Figure 15 – SEM micrographs of wear scars from the cyclic sweep tests (x1000 magnification) for (a) 0.5N, (b) 1N, (c) 2N, (d) 3N and (e) 4N.

The SEM micrographs for 0.5N samples show signs of non-directional wear suggesting three-body rolling wear (Figure 5(a)). If the magnification of the 0.5N micrographs is increased, the signs of directional wear can be observed (Figure 15(a)). This is potentially caused by two-body grooving wear indicating a mixed wear regime at 0.5N. The SEM micrographs for 1N samples show a slight increase in two-body grooving wear, but it appeared to still be displaying a mixed regime (Figure 15(b)). For samples of 2N and higher very clear two-body grooving can be observed suggesting that by 2N the wear regime has fully transitioned to two-body wear (Figures 15(c) to (e)). These micrograph results appear to be consistent with the Adachi and Hutchings prediction for wear regime transition.

5. Conclusions

- A study of the effects of applied load and electrical potential on the micro-abrasion-corrosion mechanisms of 316L stainless steel in artificial saliva has been carried out.
- The results from the micro-abrasion-corrosion tests were used to generate polarisation curves, wastage and mechanism maps and to describe the material's tribo-corrosion behaviour in a simulated oral environment.
- It was found that the corrosion resistant nature of 316L stainless steel made its wear mechanism micro-abrasion dominated for all test conditions.
- The superior corrosion resistance of 316L stainless steel has resulted in a micro-abrasion rate to be significantly higher than corrosion rate. This was confirmed by the microscopy inspection as any visual signs of surface corrosion had been removed by the micro-abrasion mechanisms which predominate.
- The polarisation curve results displayed a significant increase in corrosion current density in the presence of abrasive particles suggesting the removal of the protective chromium oxide passive film.
- The micro-abrasion and corrosion weight loss results suggest that the rate of corrosion in anodic conditions increases with the increase of micro-abrasion.
- Repassivation phenomena were observed in the polarisation curves with higher micro-abrasion. A higher frequency of repassivation was observed for higher rates of micro-abrasion.

References

[1] J. Chen, “Food oral processing: Some important underpinning principles of eating and sensory perception,” *Food Struct.*, vol. 1, no. 2, pp. 91–105, Apr. 2014.

[2] M. Mirjalili, M. Momeni, N. Ebrahimi, and M. H. Moayed, “Comparative study on corrosion behaviour of Nitinol and stainless steel orthodontic wires in simulated saliva solution in presence of fluoride ions.,” *Mater. Sci. Eng. C. Mater. Biol. Appl.*, vol. 33, no. 4, pp. 2084–93, May 2013.

[3] C. Hodge and M. M. Stack, “Tribo-corrosion mechanisms of stainless steel in soft drinks,” *Wear*, vol. 270, no. 1, pp. 104–114, 2010.

[4] A. Kocijan, D. K. Merl, and M. Jenko, “The corrosion behaviour of austenitic and duplex stainless steels in artificial saliva with the addition of fluoride,” *Corros. Sci.*, vol. 53, no. 2, pp. 776–783, Feb. 2011.

[5] R. A. Antunes, A. C. D. Rodas, N. B. Lima, O. Z. Higa, and I. Costa, “Study of the corrosion resistance and in vitro biocompatibility of PVD TiCN-coated AISI 316L austenitic stainless steel for orthopedic applications,” *Surf. Coatings Technol.*, vol. 205, no. 7, pp. 2074–2081, Dec. 2010.

[6] D. Holmes, S. Sharifi, and M. M. Stack, “Tribo-corrosion of steel in artificial saliva,” *Tribol. Int.*, vol. 75, pp. 80–86, Jul. 2014.

[7] J. Z. Shen, A. Tampieri, J. Chevalier, H. Engqvist, J. Ferreira, E. Sánchez Vilches, P. Bowen, A. Krell, Z. Zhe, L. Wang, Y. Liu, W. Si, H. Feng, Y. Tao, and Z. Ma, “Friction and wear behaviors of dental ceramics against natural tooth enamel,” *J. Eur. Ceram. Soc.*, vol. 32, no. 11, pp. 2599–2606, 2012.

[8] D. Sun, J. A. Wharton, and R. J. K. Wood, “Micro-abrasion mechanisms of cast CoCrMo in simulated body fluids,” *Wear*, vol. 267, no. 11, pp. 1845–1855, Oct. 2009.

[9] H. Gocmez, M. Tuncer, I. Uzulmez, and O. Sahin, “Particle formation and agglomeration of an alumina–zirconia powder synthesized an supercritical CO2 method,” *Ceram. Int.*, vol. 38, no. 2, pp. 1215–1219, 2012.

[10] V. Muthukumaran, V. Selladurai, S. Nandhakumar, and M. Senthilkumar, “Experimental investigation on corrosion and hardness of ion implanted AISI 316L stainless steel,” *Mater. Des.*, vol. 31, no. 6, pp. 2813–2817, 2010.

[11] J. Chen, N. Khandelwal, Z. Liu, and T. Funami, “Influences of food hardness on the particle size distribution of food boluses,” *Arch. Oral Biol.*, vol. 58, no. 3, pp. 293–298, 2013.

[12] C. G. Telfer, M. M. Stack, and B. D. Jana, “Particle concentration and size effects on the erosion-corrosion of pure metals in aqueous slurries,” *Tribol. Int.*, vol. 53, pp. 35–44, 2012.

[13] M. M. Stack, W. Huang, G. Wang, and C. Hodge, “Some views on the construction of bio-tribo-corrosion maps for Titanium alloys in Hank’s solution: Particle concentration and applied loads effects,” *Tribol. Int.*, vol. 44, no. 12, pp. 1827–1837, 2011.

[14] S. Sharifi and M. M. Stack, “A comparison of the tribological behaviour of Y-TZP in tea and coffee under micro-abrasion conditions,” *J. Phys. D. Appl. Phys.*, vol. 46, no. 40, p. 404008, Oct. 2013.

[15] K. Marcus and C. Allen, “The sliding wear of ultrahigh molecular weight polyethylene in an aqueous environment,” *Wear*, vol. 178, no. 1–2, pp. 17–28, Nov. 1994.

[16] J. Y. Wong and J. D. Bronzino, *Biomaterials*. CRC Press, 2007, p. 296.

[17] R. I. Trezona, D. N. Allsopp, and I. M. Hutchings, "Transitions between two-body and three-body abrasive wear: influence of test conditions in the microscale abrasive wear test," *Wear*, vol. 225–229, no. null, pp. 205–214, Apr. 1999.

[18] M.-L. Jalabert-Malbos, A. Mishellany-Dutour, A. Woda, and M.-A. Peyron, "Particle size distribution in the food bolus after mastication of natural foods," *Food Qual. Prefer.*, vol. 18, no. 5, pp. 803–812, 2007.

[19] Y. Oshida, *Bioscience and Bioengineering of Titanium Materials*. Elsevier, 2013, pp. 35–85.

[20] M. M. Stack, J. Rodling, M. T. Mathew, H. Jawan, W. Huang, G. Park, and C. Hodge, "Micro-abrasion–corrosion of a Co–Cr/UHMWPE couple in Ringer's solution: An approach to construction of mechanism and synergism maps for application to bio-implants," *Wear*, vol. 269, no. 5, pp. 376–382, 2010.

[21] I. Hutchings, *Tribology, Friction and Wear of Engineering Materials*. Elsevier Limited, 1992, p. 284.

[22] M. . Stack and M. Mathew, "Micro-abrasion transitions of metallic materials," *Wear*, vol. 255, no. 1–6, pp. 14–22, Aug. 2003.

[23] M. G. Gee, A. Gant, I. Hutchings, R. Bethke, K. Schiffman, K. Van Acker, S. Poulat, Y. Gachon, and J. von Stebut, "Progress towards standardisation of ball cratering," *Wear*, vol. 255, no. 1, pp. 1–13, 2003.

[24] S. . Lim, "Recent developments in wear-mechanism maps," *Tribol. Int.*, vol. 31, no. 1, pp. 87–97, 1998.

[25] S. Amini and A. Miserez, "Wear and abrasion resistance selection maps of biological materials," *Acta Biomater.*, vol. 9, no. 8, pp. 7895–7907, 2013.

[26] K. Adachi and I. M. Hutchings, "Wear-mode mapping for the micro-scale abrasion test," *Wear*, vol. 255, no. 1, pp. 23–29, 2003.

[27] M. M. Stack, N. Corlett, and S. Zhou, "A methodology for the construction of the erosion-corrosion map in aqueous environments," *Wear*, vol. 203–204, pp. 474–488, Mar. 1997.

[28] A. R. Lansdown and A. L. Price, *Materials to Resist Wear (Materials Engineering Practice)*. Pergamon, 1986, p. 200.

[29] P. . Shipway and C. J. . Hodge, "Microabrasion of glass – the critical role of ridge formation," *Wear*, vol. 237, no. 1, pp. 90–97, 2000.

[30] M. Pourbaix, *Atlas of electrochemical equilibria in aqueous solutions*. National Association of Corrosion Engineers, 1974, p. 644.

[31] S. L. Johnson, "Surface studies of potentially corrosion resistant thin film coatings on chromium and type 316L stainless steel," Kansas State University, 2006.

[32] J. F. Archard, "Contact and Rubbing of Flat Surfaces," *J. Appl. Phys.*, vol. 24, no. 8, p. 981, Aug. 1953.

[33] B. Bera, "Adhesive Wear Theory of Micromechanical Surface Contact," *Int. J. Comput. Eng. Res.*, vol. 3, no. 3, pp. 73–78, 2013.

[34] R. V. Camerini, R. B. de Souza, F. de Carli, A. S. Pereira, and N. M. Balzaretti, "Ball cratering test on ductile materials," *Wear*, vol. 271, no. 5, pp. 770–774, 2011.

[35] R. . Trezona and I. . Hutchings, “Three-body abrasive wear testing of soft materials,” *Wear*, vol. 233, pp. 209–221, 1999.